LAWRENCE
LIVERMORE
NATIONAL
LABORATORY

LLNL-JRNL-664403

Impact of inward turbulence spreading on energy loss of edge-localized modes

C. H. Ma, X. Q. Xu

November 18, 2014

Physics of Plasmas

Disclaimer

Impact of inward turbulence spreading on energy loss of edge-localized modes

C. H. Ma,[1,2] X. Q. Xu,[2] P. W. Xi,[1,2] T. Y. Xia,[3,2] P. B. Snyder,[4] S. S. Kim,[5] and X. G. Wang[1]

[1)] *Fusion Simulation Center and State Key Laboratory of Nuclear Physics and Technology, School of Physics, Peking University, Beijing, China*

[2)] *Lawrence Livermore National Laboratory, Livermore, CA 94550*

[3)] *Institute of Plasma Physics, Chinese Academy of Sciences, Hefei, China*

[4)] *General Atomics, San Diego, CA 92186*

[5)] *WCI Center for Fusion Theory, NFRI, Korea*

Nonlinear two-fluid and gyrofluid simulations show that an ELM crash has two phases: fast initial crash of ion temperature perturbation on the Alfvén time scale and slow turbulence spreading. The turbulence transport phase is a slow encroachment of electron temperature perturbation due to the ELM event into pedestal region. Because of the inward turbulence spreading effect, the energy loss of an ELM decreases when density pedestal height increases. The Landau resonance yields the different cross phase-shift of ions and electrons. A 3+1 gyro-Landau-fluid model is implemented in BOUT++ framework. The gyrofluid simulations show that the kinetic effects have stabilizing effects on the ideal ballooning mode and the energy loss increases with the pedestal height.

I. INTRODUCTION

The physics understanding of edge localized modes (ELMs)[1] in H-mode[2] discharges is critical to improving edge particles and energy confinement and the performance of future tokamaks. The theory and the numerical implementation in codes such as ELITE[3,4] show that the type-I ELM is triggered by ideal peeling-ballooning (P-B) modes, which are driven by the large pressure gradient and current profile in the pedestal region. The BOUT++ code[5–13] has successfully simulated linear growth and nonlinear crash phase of ELMs in circular and advanced divertor geometries. The P-B turbulence before an ELM crash has been proven to be important for the trigger of ELMs[14,15]. But the turbulence transport and relaxation process after the initial crash is rarely studied. We find that the inward turbulence spreading after the initial crash has a large impact on the energy loss of an ELM. In this paper, this issue is investigated by linear and nonlinear simulations based on our BOUT++ six-field Landau-fluid model which includes important kinetic effects such as Landau resonance on the top of the pedestal where plasmas are collisionless and kinetic effects are important.

The impact of kinetic ballooning mode (KBM), also known as Alfvénic ion temperature gradient mode (AITG), on the stability and transport is another important issue in edge plasma. The KBM has the same threshold for instability in the limit of zero ion temperature gradient ($\eta_i = 0$), and a somewhat lower threshold with finite ion temperature gradient due to the ion drift resonance[16,17]. The EPED model[18] successfully predicts the pedestal height and width in the experiments on multiple tokamaks based on the peeling-ballooning mode and KBM constraints. Several gyrokinetic analyses of pedestal instabilities[19–22] in real geometry show improved understanding on the edge fluctuations over the MHD model. However, it is difficult to run global electromagnetic gyrokinetic codes across the separatrix, which motivates the development of the global gyro-Landau-fluid model.

Gyrofluid or gyro-Landau fluid model is derived by taking velocity space moments of the gyrokinetic equation in guiding center space. The moment hierarchy is closed with closures, which is carefully chosen to model kinetic effects. Hammett and Perkins developed a closed set of fluid moment equations which represents kinetic Landau damping effect using the phase-mixing closures[23]. Dorland[24] model and Beer[25] model describe the electrostatic plasma turbulence in slab and toroidal geometries. The magnetic fluctations and non-

adiabatic passing electron dynamics are included in the Snyder and Hammett model[26]. Sugama[27] derived a gyrofluid model which describes collisionless time evolution of zonal flows in Tokamak. Despain[28] extended gyrofluid models to include nonlinear phase mixing phenomenon. An isothermal gyro-Landau-fluid (GLF) model[29,30] has been implemented in the BOUT++ framework, which shows the impact of a large density gradient on ELMs. The 3+1 gyro-Landau-fluid model based on Snyder and Hammett model[26] is implemented in BOUT++ framework, and has good agreement with the gyrokinetic results in electrostatic ITG simulations. The linear and nonlinear simulation results of KBM show that the kinetic effect has stabilizing effect on the ideal ballooning mode. The impact of pedestal height on the turbulence and energy loss of an ELM crash is investigated. The inward turbulent spreading is also observed in the 3+1 GLF simulations.

This paper is organized as follows: In Sec. II, we will show the 6-field Landau fluid model used in the simulation. In Sec. III, the inward turbulence spreading will be discussed. In Sec. IV, we will introduce the 3+1 gyro-Landau-fluid model implemented in the BOUT++ framework. In Sec. V, we will show the ITG and KBM simulation results. In Sec. VI, we will present summaries and discuss the future work.

II. 6-FIELD LANDAU-FLUID MODEL

Our 6-field Landau fluid model is extended from the 6-field model[5] and consists of 6 evolving equations. In the Landau fluid model, we replace the flux-limited Spitzer-Harm parallel heat flux with the Landau damping closures[23], which catch the parallel wave-particle resonance in the weakly collisional regime. The equations of 6-field Landau-fluid model written in drift order are

$$\begin{aligned}\frac{\partial}{\partial t}\varpi =& -\frac{1}{B_0}\boldsymbol{b}\times\nabla_\perp\Phi\cdot\nabla\varpi + B_0^2\nabla_\parallel\left(\frac{J_\parallel}{B_0}\right)\\ &+2\boldsymbol{b}\times\boldsymbol{\kappa}\cdot\nabla P_1 - \frac{1}{2\Omega_i}\left[\frac{1}{B_0}\boldsymbol{b}\times\nabla P_i\cdot\nabla\left(\nabla_\perp^2\Phi\right)\right.\\ &\left.-Z_i e B_0\boldsymbol{b}\times\nabla n_i\cdot\nabla\left(\frac{\nabla_\perp\Phi}{B_0}\right)^2\right]\\ &+\frac{1}{2\Omega_i}\left[\frac{1}{B_0}\boldsymbol{b}\times\nabla\Phi\cdot\nabla\left(\nabla_\perp^2 P_i\right)\right.\end{aligned}$$

$$
\begin{aligned}
&-\nabla_\perp^2\left(\frac{1}{B_0}\boldsymbol{b}\times\nabla\Phi\cdot\nabla P_i\right)\Big] + \mu_{\parallel i}\nabla_{\parallel 0}^2\varpi, && (1)\\
\frac{\partial}{\partial t}n_i =& -\frac{1}{B_0}\boldsymbol{b}\times\nabla_\perp\Phi\cdot\nabla n_i - \frac{2n_i}{B_0}\boldsymbol{b}\times\boldsymbol{\kappa}\cdot\nabla\Phi\\
&-\frac{2}{Z_i e B_0}\boldsymbol{b}\times\boldsymbol{\kappa}\cdot\nabla P_i - n_i B_0\nabla_\parallel\left(\frac{V_{\parallel i}}{B_0}\right), && (2)\\
\frac{\partial}{\partial t}V_{\parallel i} =& -\frac{1}{B_0}\boldsymbol{b}\times\nabla_\perp\Phi\cdot\nabla V_{\parallel i} - \frac{1}{m_i n_{i0}}\boldsymbol{b}\cdot\nabla P, && (3)\\
\frac{\partial}{\partial t}A_\parallel =& -\nabla_\parallel\Phi + \frac{1}{e n_{e0}}\nabla_\parallel P_e + \frac{\eta}{\mu_0}\nabla_\perp^2 A_\parallel - \frac{\eta_H}{\mu_0}\nabla_\perp^4 A_\parallel, && (4)\\
\frac{\partial}{\partial t}T_i =& -\frac{1}{B_0}\boldsymbol{b}\times\nabla_\perp\Phi\cdot\nabla T_i\\
&-\frac{2}{3}T_i\left[\left(\frac{2}{B_0}\boldsymbol{b}\times\boldsymbol{\kappa}\right)\cdot\left(\nabla\Phi + \frac{1}{Z_i e n_{i0}}\nabla P_i\right.\right.\\
&\left.\left.+\frac{5}{2}\frac{k_B}{Z_i e}\nabla T_i\right) + B_0\nabla_\parallel\left(\frac{V_{\parallel i}}{B_0}\right)\right]\\
&+\frac{2}{3 n_{i0} k_B}\nabla_{\parallel 0} q_{\parallel i} + \frac{2m_e}{m_i}\frac{Z_i}{\tau_e}\left(T_e - T_i\right), && (5)\\
\frac{\partial}{\partial t}T_e =& -\frac{1}{B_0}\boldsymbol{b}\times\nabla_\perp\Phi\cdot\nabla T_e\\
&-\frac{2}{3}T_e\left[\left(\frac{2}{B_0}\boldsymbol{b}\times\boldsymbol{\kappa}\right)\cdot\left(\nabla\Phi - \frac{1}{e n_{e0}}\nabla P_e\right.\right.\\
&\left.\left.-\frac{5}{2}\frac{k_B}{e}\nabla T_e\right) + B_0\nabla_\parallel\left(\frac{V_{\parallel e}}{B_0}\right)\right] + \frac{2}{3 n_{i0} k_B}\nabla_{\parallel 0} q_{\parallel e}\\
&-\frac{2m_e}{m_i}\frac{Z_i}{\tau_e}\left(T_e - T_i\right) + \frac{2}{3 n_{e0} k_B}\eta J_\parallel^2. && (6)
\end{aligned}
$$

The variables in these equations are defined as

$$
\begin{aligned}
\varpi =& n_{i0}\frac{m_i}{B_0}\left(\nabla_\perp^2\phi + \frac{1}{n_{i0}}\nabla_\perp\phi\cdot\nabla_\perp n_{i0} + \frac{1}{n_{i0} Z_i e}\nabla_\perp^2 p_{i1}\right), && (7)\\
J_\parallel =& J_{\parallel 0} - \frac{1}{\mu_0}\nabla_\perp^2 A_\parallel, && (8)\\
V_{\parallel e} =& V_{\parallel i} + \frac{1}{\mu_0 Z_i e n_i}\nabla_\perp^2 A_\parallel. && (9)
\end{aligned}
$$

Here $\Omega_i = Z_i eB/m_i$ is the ion gyro frequency, $\nabla_\parallel F = B\partial_\parallel(F/B)$, $\boldsymbol{\kappa} = \boldsymbol{b_0}\cdot\nabla\boldsymbol{b_0}$, $\nabla_\parallel = \nabla_{\parallel 0} - \boldsymbol{b}_0\times\nabla(A_\parallel/B)\cdot\boldsymbol{\nabla}$ and $\nabla_{\parallel 0} = \boldsymbol{b}_0\cdot\boldsymbol{\nabla}$. The definition of pressure in this model is $P_j = P_{j0} + P_{j1} = k_B n_j T_j$, $P_{j1} = k_B(n_{j0}T_{j1} + n_{j1}T_{j0} + n_{j1}T_{j1})$ for j species. The terms in two square brackets in Eq. (1) represent the gyro-viscous terms brought in by the finite ion Larmor radius effects. These terms are necessary for two-fluid models to keep the whole

finite Larmor radius stabilizing effects when ion density gradient is steep and temperature is high. The term $(1/en_{e0})\nabla_\parallel P_e$ in Eq. (4) is the electron drift wave term. η is the parallel Spitzer resistivity, $\eta_{SP} = 0.51\times1.03\times10^{-4}Z_i \ln\Lambda T^{-3/2}\Omega\cdot\mathrm{m}$ and $\eta_H = 1\times10^{-13}\mu_0 R_0^3 V_A$ is the hyper-resistivity, which remains the same for all inward turbulence spreading simulations.

The parallel heat flux in ion (5) and electron (6) temperature equations is closed by the Landau damping closures[23]:

$$q_{\parallel j} = -n_0\sqrt{\frac{8}{\pi}}v_{T_{\parallel j}}\frac{ik_\parallel}{|k_\parallel|}T_{\parallel j}, \quad j = i, e, \tag{10}$$

Here the parallel wave-particle resonances associated with perturbed magnetic field and the collisions are neglected. Because of the large spatial inhomogeneities in the edge, a new non-Fourier method is used for the calculation of the Landau-fluid operators[29,31].

The six-field equations are solved using a field-aligned (flux) coordinate system (x, y, z) with the shifted radial derivatives[32]. In this coordinate system x is the radial direction and is defined as $x = (\psi - \psi_{\mathrm{axis}})/(\psi_{\mathrm{separatrix}} - \psi_{\mathrm{axis}})$, which is the normalized poloidal flux and ψ is the poloidal magnetic flux; y is the parallel direction of the magnetic field with a twisted-shift boundary condition and z is the bi-normal direction with periodic boundary condition. The difference methods used in x and y directions are 4th-order central differencing and 3rd-order WENO[33] advection scheme for advection terms. The Fourier decomposition is used in z direction when the vorticity is inverted to get potential. The Arakawa scheme[34] is used for the magnetic flutter term $\tilde{\boldsymbol{b}}\cdot\nabla f = -[A_\parallel, f]$. The system is advanced via a fully implicit scheme PVODE[35]. The resolutions in the x and y directions are 516×64 in all the linear and nonlinear simulations. For linear simulations, the grid number in the z direction is $n_z = 17$ and $1/N_\zeta$ torus is simulated for efficiency. Here N_ζ is the toroidal mode number simulated in the linear run. For nonlinear simulations, $n_z = 65$ in one-fifth torus $N_\zeta = 5$.

III. NONLINEAR DENSITY PEDESTAL HEIGHT SCAN AND INWARD TURBULENCE SPREADING

In order to study the nonlinear evolution of the system, we keep the linear characteristics of the system about the same in the density pedestal scan. The pressure profile, the density pedestal width, the density and temperature at the peak gradient position are fixed because the linear growth rate of P-B mode is mainly determined by the local value and gradient.

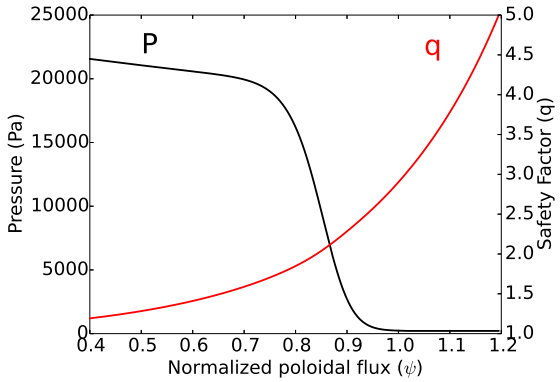

FIG. 1. Equilibrium profiles of pressure and safety factor. Black line for pressure P_0 and red line for safety factor q.

In the scan, we use a shifted circular cross-section toroidal equilibrium with an aspect ratio of 2.9 generated by the TOQ code[36]. The parameters of this equilibrium are minor radius $a = 1.17$m, major radius $R_0 = 3.44$m, magnetic field on axis $B_0 = 1.99$T and $q_{95} = 2.57$.

The equilibrium pressure and safety factor is shown in Fig. 1. In the scan, the equilibrium pressure profile P_0 is separated into ion density n_{i0}, ion and electron temperature T_{i0} and T_{e0}. From the quasi-neutrality condition, $Z_i n_{i0} = n_{e0}$, where Z_i is ion charge and n_{e0} is the equilibrium electron density. In all our simulations, we assume $T_{i0} = T_{e0}$ and we choose the analytical profiles of n_{i0} as

$$n_{i0}(x) = \left[A \times \tanh\left(\frac{x - x_{\rm ped}}{\Delta_n/2}\right) + B\right] \times n_{\rm ped}. \tag{11}$$

We define $n_{\rm height} = A + B$ and $n_{\rm offset} = B - A$. Here $n_{\rm ped}$ is the ion number density on the top of the pedestal region, $n_{\rm offset}$ is the ratio to control the bottom amplitude of n_{i0} outside the separatrix, and $n_{\rm height}$ is the coefficient to specify the pedestal height of n_{i0}. In all our cases, we have $n_{\rm ped} = 10^{20}{\rm m}^{-3}$, $x_{\rm ped} = 0.633$ and $\Delta_n = 0.2$. The coefficients A and B used in our scan for Eq. (11) are listed in table I. Because the pressure profile is unchanged, the temperature pedestal height and width decrease when the density pedestal height increases.

First, we study the effect of Landau resonance in the inward turbulence spreading. For simplicity, the 6-field model is reduced to a 3-field like model, and we only keep the $E \times B$ advection terms in the ion and electron temperature equations and set $V_{\|i} = 0$ to remove the compression effects. When we reduce the 6-field model to the 3-field like model, the ion and electron equations are still separate and the Landau closures are kept as in Eq. (10). Fig. 2 shows the time evolution of the turbulence intensity without Landau resonance effects. It

TABLE I. Coefficients of three density profiles.

	n_{height}	n_{ave}	A	B
Case 1	0.600	0.200	0.200	0.400
Case 2	0.520	0.280	0.120	0.400
Case 3	0.454	0.345	0.054	0.400

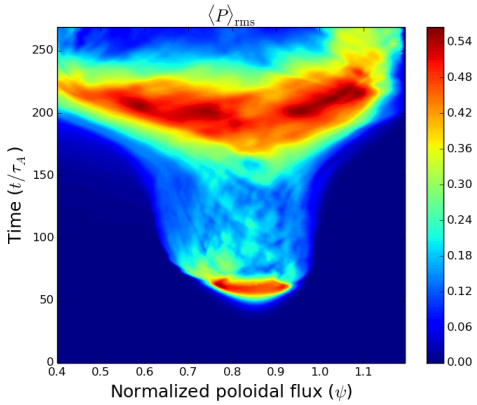

FIG. 2. The time evolution of the turbulence intensity: the root-mean-squared pressure perturbations for the case without Landau closures.

shows that the initial crash happens around $t = 60\tau_A$. The turbulence spreading is observed around $t = 170\tau_A$ after the initial crash and soon reaches the boundary, and yields a large energy loss. That means the nonlinear $E \times B$ advection causes the turbulence spreading effect. Fig. 3 shows the effect of Landau resonance in the reduced model. The energy loss ratio is defined as

$$\Delta_{\text{ped}}^{\text{th}} = \frac{\Delta W_{\text{PED}}}{W_{\text{PED}}} = \frac{\left\langle \int_{R_{\text{in}}}^{R_{\text{out}}} \oint dR d\theta (P_0 - \langle P \rangle_\xi) \right\rangle_t}{\int_{R_{\text{in}}}^{R_{\text{out}}} \oint dR d\theta P_0}. \tag{12}$$

The ion and electron perturbations are the same for the case without Landau resonance effects. The Landau resonance effects suppress the turbulence spreading and reduce the total energy loss. The Landau resonance effects also produce the different responses to ions and electrons. The energy loss from electrons is larger than the energy loss from ions due to the Landau resonance effects.

When pressure profile is fixed, the linear growth rates are about the same for these cases because the density and temperature value is fixed at the peak gradient position

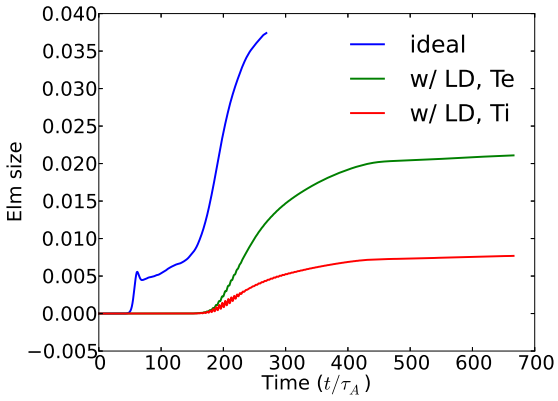

FIG. 3. Time evolution of ELM size for reduced model. The blue line for the case without Landau closures, the green and red line for the case with Landau closures. The green line for electrons and the red line for ions.

at $\psi = 0.85$. Although the linear growth rates are about the same for these cases, our nonlinear simulations show that the density and temperature profiles have a large impact on the nonlinear evolution of the turbulence. Fig. 4 shows the nonlinear evolution of electron temperature perturbations on the outer mid-plane. (a)-(c) for $n_{\text{height}} = 0.60$; (d)-(f) for $n_{\text{height}} = 0.52$; (g)-(i) for $n_{\text{height}} = 0.45$. The filamentary structure is observed at the time of initial crash ($t = 100\tau_A$). The mode number and width of the filamentary structures for different cases are about the same from the similar linear drives. After that, the inverse cascade of the turbulence transfers energy to lower mode number. For low density cases, the inverse cascade effect is stronger and introduces the inward turbulence spreading, and the perturbations spread inward to the top of the pedestal, shown in Fig. 4 (f) and (i). The energy loss from the inward turbulence spreading eventually dominates the total energy loss of an ELM.

Fig. 5 compares the energy loss vs. the pedestal density height from different channels. The conductive energy loss is dominant in these cases while the convective energy loss remains small. When the pedestal density height increases, the conductive energy loss from the electron temperature perturbations decreases because of the inward turbulence spreading, which is consistent with the DIII-D experimental results[37]. The conductive energy loss from the ion temperature perturbations also decreases. But the impact of pedestal density height on the ion temperature perturbations is small, because the linear drives are the same and there is no spreading effects for ions. The convective energy loss from density

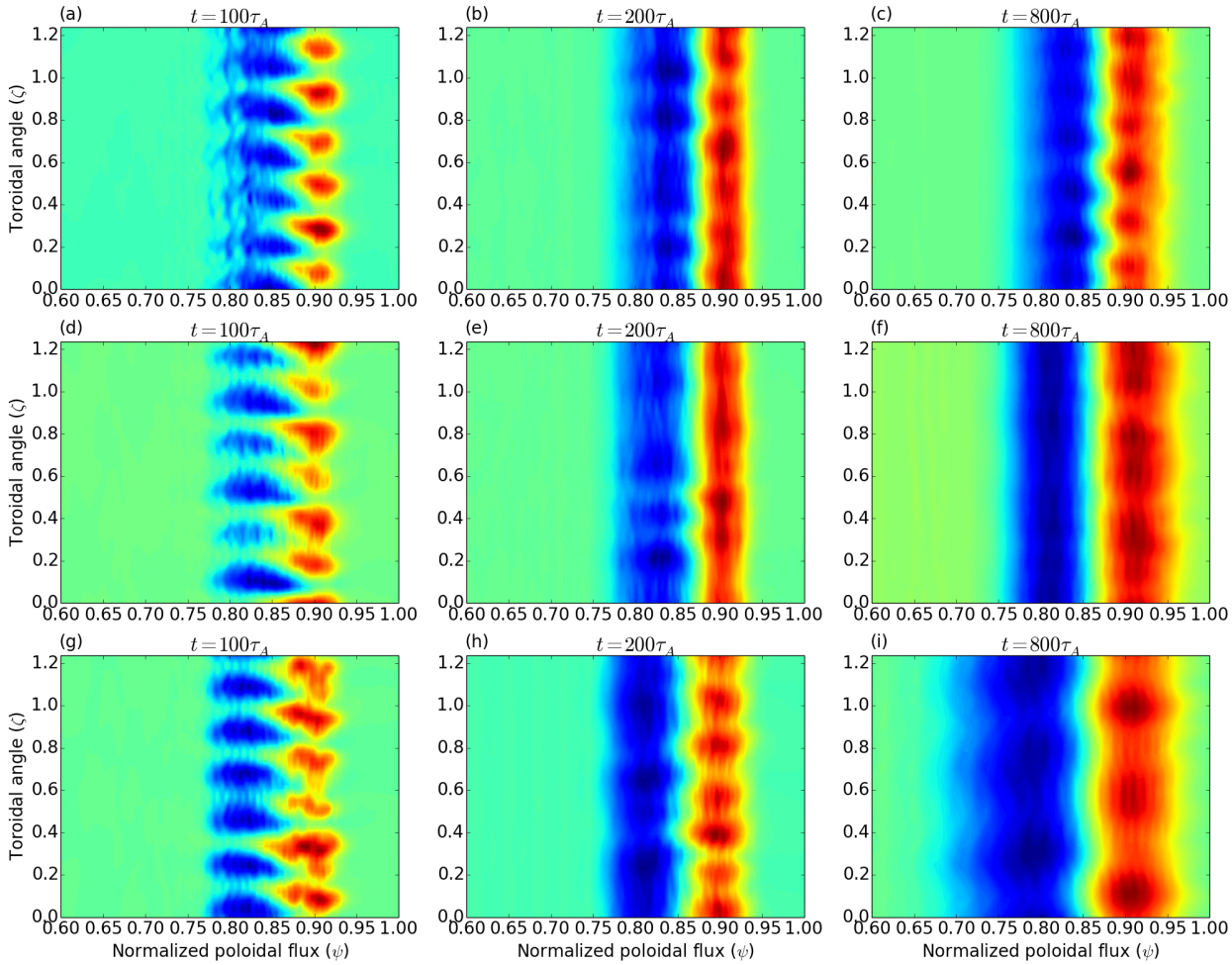

FIG. 4. Electron temperature perturbation on the outer mid-plane for different cases at different time. (a)-(c) for $n_{\rm height} = 0.60$; (d)-(f) for $n_{\rm height} = 0.52$; (g)-(i) for $n_{\rm height} = 0.45$. The toroidal segment is 5.

perturbations is large when the density pedestal height and gradient is large.

Fig. 6 shows the cross-phase shift between perturbations and the $E \times B$ velocity. The cross-phase shift is defined as

$$\alpha_j(\psi, \theta, n, t) = arg\left[\frac{\hat{v}_{E,n}(\psi, \theta, t)}{\hat{T}_{j,n}(\psi, \theta, t)}\right], \alpha_j \in (-\pi, \pi], \tag{13}$$

where $j = i, e$ for different species, and $\hat{v}_{E,n}$ and $\hat{T}_{j,n}$ are the nth toroidal Fourier component of v_E and T_j. The phase-shift is a predominant effect induced by the electron Landau closure in Eq. (14).

$$\tilde{T}_e = \frac{\omega_{*T_e}}{\omega + \Delta\omega + i\chi_{\parallel e}k_\parallel^2}\tilde{\phi}, \tag{14}$$

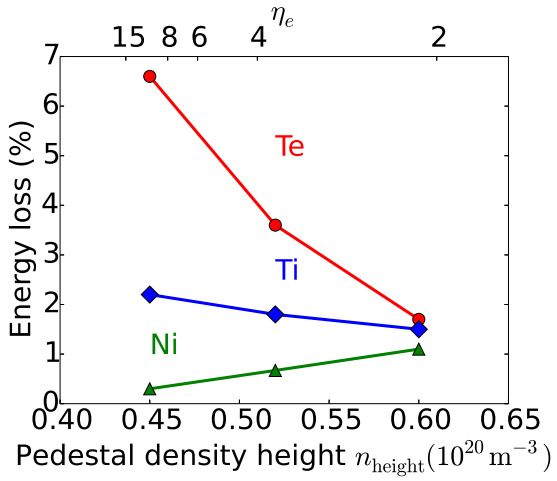

FIG. 5. Comparison of the energy loss vs. pedestal density height from different channels. The red line for electron temperature; the blue line for ion temperature and the green line for density.

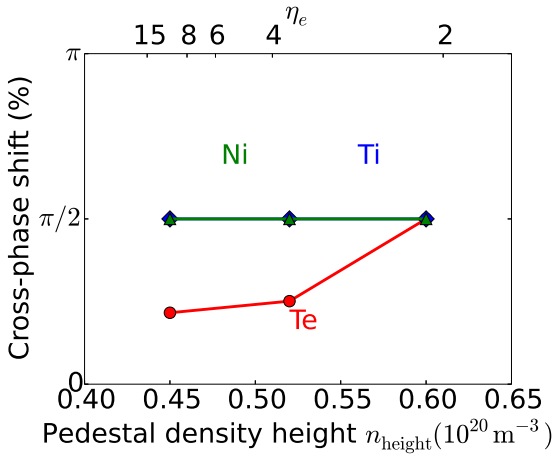

FIG. 6. Comparison of the time-averaged cross-phase shift vs. pedestal density height from different channels during the spreading phase. The red line for electron temperature; the blue line for ion temperature and the green line for density.

$$\tilde{T}_i \simeq \frac{\omega_{*T_i}}{\omega + \Delta\omega}\tilde{\phi}. \tag{15}$$

Here $\Delta\omega$ labels the frequency and phase shift from the nonlinear effect and $i\chi_{\parallel e}k_\parallel^2$ is the effect of electron Landau resonance. In Eq. (15), the ion Landau resonance effect is neglected because the following inequalities are satisfied for pedestal plasmas, $\chi_{\parallel i}k_\parallel^2 \ll \omega \sim \chi_{\parallel e}k_\parallel^2$, where $\chi_{\parallel i}$ and $\chi_{\parallel e}$ are the equivalent parallel conductivities in the Landau closures Eq. (10). From Eq. (10), we find that $\chi_{\parallel e} \propto v_{T_{\parallel e}} \propto \sqrt{T_e}$. When the pedestal density height decreases

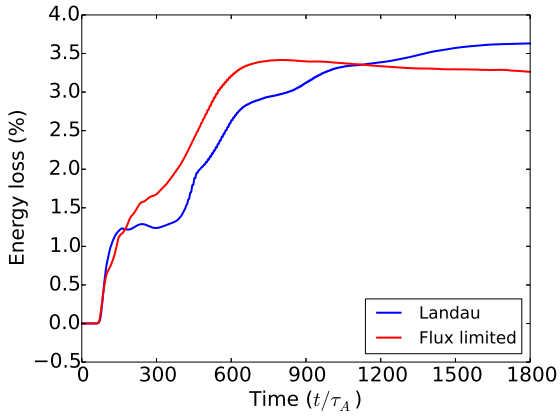

FIG. 7. Time evolution of the energy loss of electron perturbations for different parallel closures. Blue line for Landau damping closures; red line for flux limited expressions.

and the pedestal temperature height increases, the electron Landau resonance effect becomes stronger, which induces a smaller cross-phase shift of electrons and larger difference between electrons and ions, shown in Fig. 6. The ion Landau resonance effect is small and neglected in Eq. (15). So the cross-phase shift of ions remains the same during the scan. The same is true for density. The cross-phase shift induces a radial transport[38], which is

$$\langle v_E T_j \rangle = \sum_n |v_{E-n}||T_{j_n}| \cos \alpha_{j_n} \tag{16}$$

and eventually yields a large turbulence spreading and energy loss from the electron temperature perturbations, while the density and ion temperature perturbations have no spreading at all.

In Braginskii's two-fluid model, the classical thermal conductivities are defined as,

$$q_{\|i} = \kappa_{\|i}^{\mathrm{SH}} \nabla_\| T_i, \tag{17}$$

$$q_{\|e} = \kappa_{\|e}^{\mathrm{SH}} \nabla_\| T_e, \tag{18}$$

where $\kappa_{\|i}^{\mathrm{SH}} = 3.9 n_i v_{th,i}^2/\nu_i$ and $\kappa_{\|e}^{\mathrm{SH}} = 3.2 n_e v_{th,e}^2/\nu_e$ are the classical parallel thermal conductivities, where $v_{th,j}$ is the thermal velocity for j particle and ν_j is the collision rate. In the hot pedestal region, the collisionality is low and the classic $\kappa_{\|j}$ is not valid for weakly collisional plasmas. In previous two fluid simulations[5], the kinetic effect is taken into accounts by using the free-streaming expression $\kappa_j^{\mathrm{FS}} = \alpha_j n_j v_{\mathrm{th},j} q R_0$, where q is the local safety factor.

The effective thermal conductivities (flux limited expression) are written as

$$\kappa_{\mathrm{eff},j} = \frac{\kappa_{\|j}^{\mathrm{SH}} \kappa_j^{\mathrm{FS}}}{\kappa_{\|j}^{\mathrm{SH}} + \kappa_j^{\mathrm{FS}}}. \tag{19}$$

With this expression, $\kappa_{\mathrm{eff},j}$ is limited by κ_j^{FS} on the core region where mean free path is high, and is determined by $\kappa_{\|j}^{\mathrm{SH}}$ at the bottom of the pedestal region where the plasmas are collisional. Under the long wave-length assumption, we can assume that $|k_\|| \approx 1/qR_0$, $ik_\| = \nabla_{\|0}$. The only difference between Eq. (10) and (19) is the coefficient α_j. So the flux limited expression in Eq. (19) is a good approximation of Landau damping closures, but it includes collision effect in the cold region. Fig. 7 shows the comparison of Landau damping closures and flux limited expressions. From the plot, we can see that the linear drives are the same for different closures. The inward spreading effect is observed in the simulation with flux limited expressions, too. The spreading speed is faster than the case with Landau damping closures while the saturated energy loss is similar. The closures do not change the radial correlation of the turbulence, which causes the spreading.

IV. GLOBAL 3+1 GYRO-LANDAU-FLUID MODEL

Our global 3+1 gyro-Landau-fluid (GLF) model is utilized from the Snyder-Hammett gyrofluid model[26] by (1) adding the full electron temperature (T_e) responses; (2) adding the cross term $\frac{e\rho_i^2}{T_0}\nabla n_0 \cdot \nabla(\Gamma_0 - \Gamma_1)\phi$ in the Poisson equation which is important when the density gradient is large[39]; (3) adding the hyper-resistivity η_i in the Ohm's Law[6]; (4) using the vorticity formulations $\tilde{\varpi}_G = eB(\tilde{n}_e - \tilde{n}_i)$. The 3+1 means it includes three parallel moment equations and one perpendicular moment equation of each species.

The GLF model consists of 7 evolving equations:

$$\begin{aligned}
\frac{\partial \tilde{n}_i}{\partial t} =& -\frac{1}{B_0} b_0 \times \nabla\Phi \cdot \nabla n_i - \frac{1}{eB_0} b_0 \times \kappa \cdot \nabla(p_{\|i} + p_{\perp i}) \\
& - \frac{n_i}{B_0} b_0 \times \kappa \cdot \nabla \left(2 + \frac{1}{2}\hat{\nabla}_\perp^2\right)\Phi - n_0 B_0 \tilde{\nabla}_\| \frac{\tilde{u}_{\|i}}{B_0} - \frac{n_0}{2T_0 B_0} b_0 \times \nabla\left(\hat{\nabla}_\perp^2 \Phi\right) \cdot \nabla T_{\perp i}, \qquad (20) \\
\frac{\partial \tilde{u}_{\|i}}{\partial t} =& -\frac{1}{B_0} b_0 \times \nabla\Phi \cdot \nabla \tilde{u}_{\|i} - \frac{B_0}{n_0 m_i} \tilde{\nabla}_\| \frac{\tilde{p}_\|}{B} - \frac{4}{eB_0} b_0 \times \kappa \cdot \nabla T_{i0} \tilde{u}_{\|i} \\
& - \left(\frac{\tilde{p}_{\perp i}}{n_0 m_i} + \frac{e}{2m_i}\hat{\nabla}_\perp^2 \Phi\right) \nabla_\| \log B_0 - \frac{1}{p_{i0}} i\omega_d (\tilde{q}_{\|i} + \tilde{q}_{\perp i}), \qquad (21) \\
\frac{\partial \tilde{p}_{\|i}}{\partial t} =& -\frac{1}{B_0} b_0 \times \nabla\Phi \cdot \nabla p_{\|i} - \frac{n_0}{2B_0} b_0 \times \nabla\left(\hat{\nabla}_\perp^2 \Phi\right) \cdot \nabla T_{\perp i}
\end{aligned}$$

$$- \frac{p_{\|i}}{B_0} b_0 \times \kappa \cdot \nabla \left(4 + \frac{1}{2}\hat{\nabla}_\perp^2\right) \Phi - 3B_0 \tilde{\nabla}_\| \frac{p_{i0}\tilde{u}_{\|i}}{B_0} - i\omega_d(\tilde{r}_{\|,\|} + \tilde{r}_{\|,\perp}) - B_0 \nabla_{\|0} \frac{\tilde{q}_{\|i}}{B_0}, \quad (22)$$

$$\frac{\partial \tilde{p}_{\perp i}}{\partial t} = - \frac{1}{B_0} b_0 \times \nabla \Phi_2 \cdot \nabla p_{\perp i} - \frac{n_0}{B_0} b_0 \times \left(\hat{\hat{\nabla}}_\perp^2 \Phi\right) \cdot \nabla T_{\perp i}$$
$$- \frac{p_{\perp i}}{B_0} b_0 \times \kappa \cdot \nabla \left(3 + \frac{3}{2}\hat{\nabla}_\perp^2 + \hat{\hat{\nabla}}_\perp^2\right) \Phi - B_0^2 \tilde{\nabla}_\| \frac{p_{\perp i}\tilde{u}_{\|i}}{B_0^2} - i\omega_d(\tilde{r}_{\|,\perp} + \tilde{r}_{\perp,\perp}) - B_0^2 \nabla_{\|0} \frac{\tilde{q}_{\perp i}}{B_0^2},$$

please define P||e and Pperpe

$$\frac{\partial \tilde{\varpi}_G}{\partial t} = - \frac{1}{B_0} b_0 \times \nabla \phi \cdot \nabla \varpi_G + B_0^2 \tilde{\nabla}_\| \frac{\tilde{J}_\|}{B_0} + b_0 \times \kappa \cdot \nabla (\tilde{p}_{\|i} + \tilde{p}_{\perp i} + \tilde{p}_{\|e} + \tilde{p}_{\perp e})$$
$$+ eB_0 b_0 \times \nabla \phi_f \cdot \nabla n_i + \frac{eB_0 n_0}{T_{i0}} b_0 \times \nabla \left(\hat{\nabla}_\perp^2 \Phi\right) \cdot \nabla T_{\perp i}$$
$$+ eB^2 (\delta \bar{\boldsymbol{b}} - \delta \boldsymbol{b}) \cdot \nabla \frac{n_0 u_{\|i}}{B_0} + en_0 b_0 \times \kappa \cdot \nabla \left(2\phi_f + \hat{\nabla}_\perp^2 \Phi\right), \quad (24)$$

Please define p||e

$$\frac{\partial A_\|}{\partial t} = - \tilde{\nabla}_\| \phi + \frac{B_0}{n_0 e} \tilde{\nabla}_\| \frac{\tilde{p}_{\|e}}{B_0} + \frac{\eta}{\mu_0} \nabla_\perp^2 A_\| - \frac{\eta_H}{\mu_0} \nabla_\perp^4 A_\|, \quad (25)$$

$$\frac{\partial \tilde{T}_e}{\partial t} = - \frac{1}{B_0} b \times \nabla_\perp \phi \cdot \nabla \tilde{T}_e - \frac{2}{3} T_e \left[\left(\frac{2}{B_0} b \times \kappa\right) \cdot \left(\nabla \phi - \frac{1}{en_{e0}} \nabla \tilde{P}_e \right.\right.$$
$$\left.\left. - \frac{5}{2e} \nabla \tilde{T}_e\right) + B_0 \nabla_\| \left(\frac{\tilde{u}_{\|e}}{B_0}\right)\right] + \frac{2}{3n_{i0}} \nabla_{\|0} q_{\|e}$$

Please check where is the mirror term, the last term of Eq.(3.105) on page 73 in Snyder thesis? In collisional case, there is a similar term in your reference 7 and 8, for example please see Eq.(2.10) in Eq.(2.1) in reference 8.

where

$$\tilde{\varpi}_G = eB \left[\bar{n}_i - \tilde{n}_i - n_0 (1 - \Gamma_0) \frac{e\phi}{T_0} + \frac{e\rho_i^2}{T_0} \nabla n_0 \cdot \nabla (\Gamma_0 - \Gamma_1)\phi\right], \quad (27)$$

$$\tilde{J}_\| = -\frac{1}{\mu_0} \nabla_\perp^2 A_\| = en_0 (\bar{u}_{\|i} - \tilde{u}_{\|e}). \quad (28)$$

The gyro-averaged potentials are defined as $\Phi = \Gamma_0^{1/2}\phi$, $\phi_f = \Phi - \phi$, and $\bar{A}_\| = \Gamma_0^{1/2} A_\|$. Here, $\tilde{\nabla}_\| = \nabla_{\|0} - b_0 \times \nabla A_\| \cdot \nabla / B$, and the modified Laplacian operators $\hat{\nabla}_\perp^2$ and $\hat{\hat{\nabla}}_\perp^2$ are defined as

$$\hat{\nabla}_\perp^2 \Phi = 2b \frac{\partial \Gamma_0^{1/2}}{\partial b} \phi, \quad (29)$$

$$\hat{\hat{\nabla}}_\perp^2 \Phi = b \frac{\partial^2}{\partial b^2} (b\Gamma_0^{1/2}) \phi, \quad (30)$$

where, $b = -\rho_i^2 \nabla_\perp^2$.

The temperatures are defined as $T_j = T_{j0} + \tilde{T}_j, \tilde{T}_j = (\tilde{p}_j - \tilde{n}_j T_{j0})/(n_0 + \tilde{n}_j)$ for j species. $\bar{n}_i$ and $\bar{u}_{\|i}$ are the gyro-phase independent part of the real space ion density and parallel velocity. They are defined as

$$\bar{n}_i = \Gamma_0^{1/2} \tilde{n}_i + \frac{n_0}{T_0} b \frac{\partial}{\partial b} \Gamma_0^{1/2} \tilde{T}_{\perp i}, \quad (31)$$

$$\bar{u}_{\parallel i} = \Gamma_0^{1/2} u_{\parallel i}. \tag{32}$$

The modified Bessel functions are implemented in BOUT++ framework by using Padé approximation, which are $\Gamma_0^{1/2}(b) = 1/(1+b/2), \Gamma_0 - \Gamma_1 = 1$.

These equations are closed by Landau damping closures

$$\tilde{q}_{\parallel i} = -n_0 \sqrt{\frac{8}{\pi}} v_{T_{th,i}} \frac{ik_\parallel \tilde{T}_{\parallel i}}{|k_\parallel|}, \tag{33}$$

$$\tilde{q}_{\perp i} = -n_0 \sqrt{\frac{2}{\pi}} v_{T_{th,i}} \frac{ik_\parallel}{|k_\parallel|} \left(\tilde{T}_{\perp i} + \frac{e}{2} \hat{\nabla}_\perp^2 \Phi \right), \tag{34}$$

$$\tilde{q}_{\parallel e} = -n_0 \sqrt{\frac{8}{\pi}} v_{T_{th,e}} \frac{ik_\parallel \tilde{T}_{\parallel e}}{|k_\parallel|}. \tag{35}$$

please define T||e

and toroidal closures[40]

$$i\omega_d \left(\tilde{r}_{\parallel,\parallel} + \tilde{r}_{\parallel,\perp} \right) = i\omega_d \left(7\tilde{p}_\parallel + \tilde{p}_\perp - 4T_0 \tilde{n} - 2i \frac{|\omega_d|}{\omega_d} \left(\nu_1 \tilde{T}_\parallel + \nu_2 \tilde{T}_\perp \right) \right), \tag{36}$$

$$i\omega_d \left(\tilde{r}_{\parallel,\perp} + \tilde{r}_{\perp,\perp} \right) = i\omega_d \left(\tilde{p}_\parallel + 5\tilde{p}_\perp - 3T_0 \tilde{n} - 2i \frac{|\omega_d|}{\omega_d} \left(\nu_3 \tilde{T}_\parallel + \nu_4 \tilde{T}_\perp \right) \right), \tag{37}$$

$$i\omega_d \left(\tilde{q}_{\parallel i} + \tilde{q}_{\perp i} \right) = 2n_0 T_0 \nu_5 |\omega_d| \tilde{u}_{\parallel i},$$

Phil Snyder said that these coefficients are mass independent and they are the same for electrons and ions. Please check from Beer's thesis.

where

$$\nu = \nu_r + i\nu_i \frac{|\omega_d|}{\omega_d} \Rightarrow \begin{cases} \nu_1 &= (1.232, 0.437) \\ \nu_2 &= (-0.912, 0.362) \\ \nu_3 &= (-1.164, 0.294) \\ \nu_4 &= (0.478, -1.926) \\ \nu_5 &= (0.515, -0.958) \end{cases} \tag{39}$$

This set of equations describes the nonlinear evolution of kinetic ballooning modes (KBM) with the full FLR effects up to $k_\perp \rho_i \approx 1$.

V. GYRO-LANDAU FLUID SIMULATION RESULTS

A. Electrostatic ITG simulations

To verify our 3+1 GLF model, we perform the ITG simulations in the electrostatic regime where $\beta_e = 0$. We use adiabatic electron response in Eq. (40) instead of evolving the set of

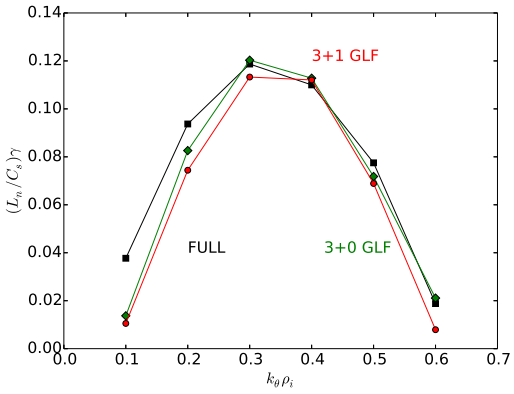

FIG. 8. Comparison of the linear growth rate of ITG between different models. Red for 3+1 GLF model, green for 3+0 gyrofluid model and black for gyrokinetic model (FULL).

electron equations in Eq. (24) - (26).

$$\frac{n_0}{T_{e0}}\tilde{\phi} + \frac{n_0}{T_{i0}}(1-\Gamma_0)\tilde{\phi} = \bar{n}_i \tag{40}$$

The equilibrium profile we used in the simulation is based on the "Cyclone base case parameter set"[41]. The parameters are $\eta_i = 3.114$, safety factor $q = 1.4$ at the peak gradient position, $R/L_T = 6.92$ where L_T are the temperature gradient scale length, and $\epsilon \equiv r/R = 0.18$. The linear growth rate of ITG is shown in Fig. 8. ITG has the largest growth rate at $k_\theta \rho_i = 0.3$. It shows that the our 3+1 GLF model has good agreement with other gyrokinetic (FULL[42]) and gyrofluid (3+0 GLF) codes.

B. Global beta scan

In this subsection, we simulate a series of different profiles of pressure. Fig. 9 shows the pressure, density, and temperature profiles used in this scan. Here, we assume $n_{i0} = n_{e0}$ and $T_{i0} = T_{e0}$. In the scan, the equilibrium temperature is fixed and the pressure and density increase proportionally to β. Eight self-consistent shifted-circular geometry grid files are generated for different pressure profiles. The parameters of these equilibria are magnetic field on axis $B_0 = 1.99$T, minor radius $a = 1.17$m, major radius $R_0 = 3.44$m, and $\eta_i = 0.685$. These cases are weakly-collisional because the pedestal collisionality $\nu_e^* = qR\epsilon^{-3/2}(\lambda_{e,e})^{-1} < 0.1$. The normalized Lundquist number for resistivity in Eq. (25) is $\eta^{-1} = 10^8$ and the normalized hyper-resistivity used in the simulation is $\eta_H = 10^{-14}$, which

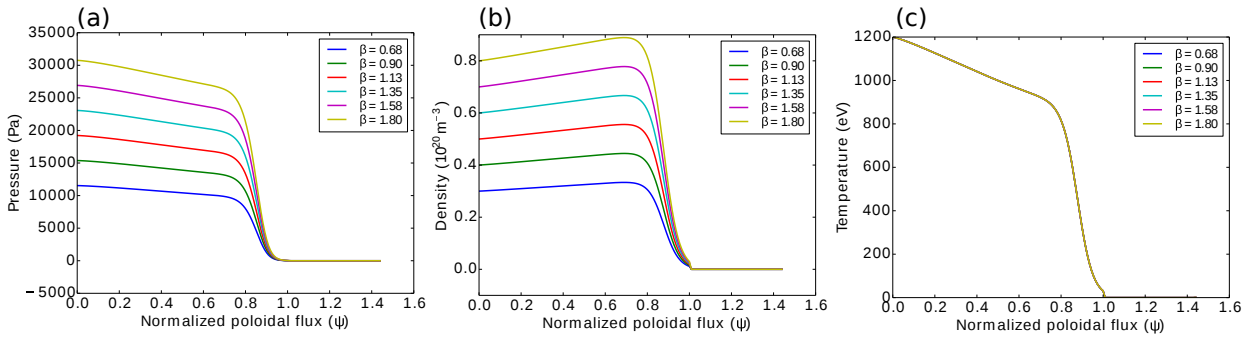

FIG. 9. Equilibrium profiles used in the beta scan. (a) for pressure; (b) for density and (c) for temperature.

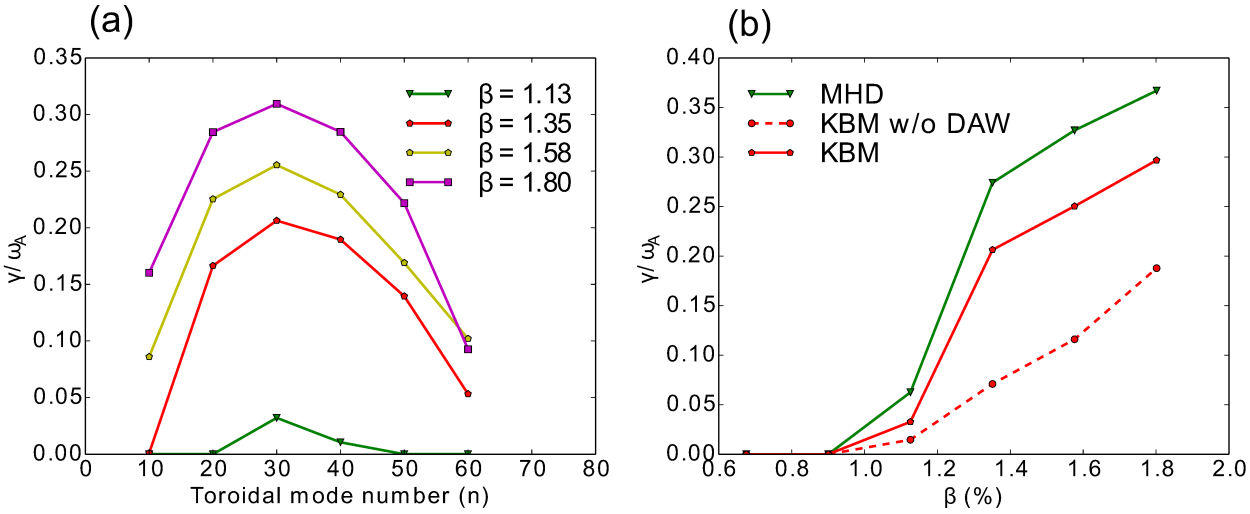

FIG. 10. (a) Linear growth rate spectrum of KBM for different β; (b) Comparison of linear growth rate vs. β. Green line for the ideal ballooning mode, red solid line for KBM and red dash line for the KBM case without drift Alfvén wave effect.

remains the same for all cases. The grid number in z direction is $n_z = 17$ for linear run and $n_z = 65$ for nonlinear run.

Fig. 10(a) shows the linear growth rate spectrum of KBM in the β scan. The KBM is unstable from the case with $\beta = 1.13\%$. The growth rate of KBM increases and the unstable region is wider when β increases. Fig. 10(b) compares the linear growth rate of the most unstable mode ($n = 30$) between ideal ballooning mode (IBM) and KBM. KBM has a smaller growth rate than that of IBM from the FLR stabilizing effects. The ion diamagnetic frequency $\omega_* = i\frac{1}{Bn_{0e}} b \times \nabla P_{i0} \cdot \nabla \propto \nabla(n_0 T_{i0})/n_0$ represents the dominant effect of FLR stabilizing effects. Here, the equilibrium temperature is fixed when we increase the density

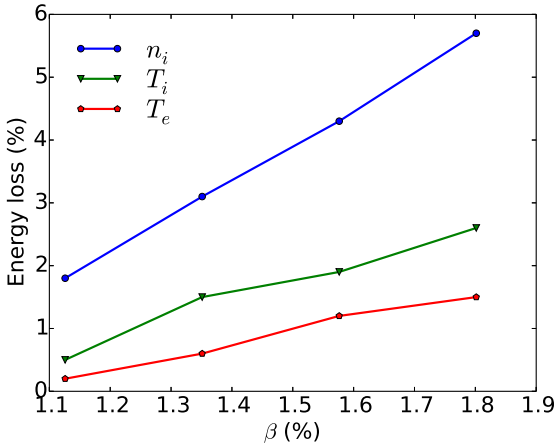

FIG. 11. Relative energy loss during the initial crash phase vs. β for different channels. Blue line for ion density; green line for ion temperature and red line for electron temperature.

and the ω_* is the same in the β scan. So the shape of the growth rate spectrum $\gamma(n)$ and the toroidal mode number n corresponding to the maximum growth rates are almost the same during the β scan, which is different from the density scan for a fixed pressure where both density and temperature changes [13]. Because the $\eta_i = 0.685$ which is too small to drive the KBM instability below the ideal ballooning unstable threshold, the unstable thresholds of IBM and KBM are similar. The red dashed line shows the effect of drift Alfvén wave (DAW). The small linear growth rate of KBM without DAW indicates that DAW has large destabilizing effects on the ballooning modes, because DAW reduces the shear Alfvén wave stabilizing effect. When we turn off the curvature drive term in Eq. (24), all the modes are stable. That means the mode is still KBM because it is driven by curvature.

Fig. 11 compares the relative energy loss from different channels during the initial crash phase in the simulations. It shows that the energy loss increases when beta increases from larger linear drive. Because η_i is relatively small in these cases, the convective energy loss from density perturbations dominates the conductive energy loss from the temperature perturbations. Remarkably, η_i determines whether conductive or convective energy loss are dominant in an ELM crash. The simulation results of our 6-field Landau fluid model for these equilibria also shows that the convective energy loss from density perturbations is dominant. On the other hand, when we perform a similar simulation for 3+1 GLF model with the equilibrium profile discussed in Sec. III in which $\eta_i > 1$, the conductive energy loss from the temperature perturbations is larger than the convective energy loss from the

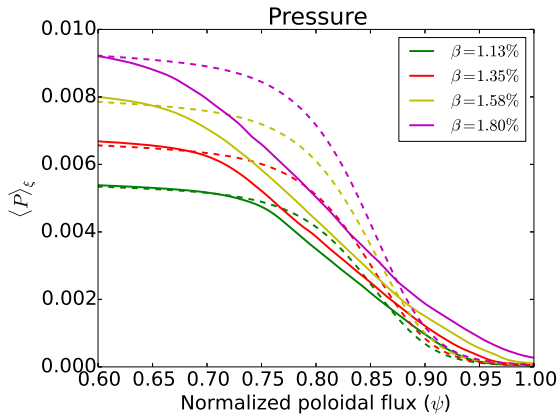

FIG. 12. Flux surface averaged total pressure profile at the outer-mid-plane of different β. The solid curves for the pressure profiles after the initial crash and the dash curves for the equilibrium pressure profiles.

density perturbations. The electron temperature perturbations are damped by the strong electron Landau resonance effect, which is larger than ions by a factor of $\sqrt{m_i/m_e}$. So the energy loss from ion temperature perturbations is larger than the energy loss from electron temperature perturbations during the initial crash phase.

Fig. 12 shows the total pressure profile after the initial crash. From the solid line in Fig. 12, we can see that the pressure profiles after the initial crash shown as solid curve have a smaller gradient than the equilibrium profiles shown as dash curve. The flattening of the profile during the initial crash has a timescale around tens of Alfvén times, which are much faster than the following turbulent transport process. When beta increases, the perturbations penetrate deeper into the top of pedestal, which means the affected volume of the ELM crash increases and yields larger energy loss.

The toroidal power spectrum of potential is shown in Fig. 13. We can see that in the KBM strongly unstable cases ($\beta = 1.35, 1.58, 1.80$), the turbulence inverse cascade effect transfers energy to low n mode, leading to a large ELM crash. In the marginal unstable case ($\beta = 1.13$) shown in Fig. 13 as green curve, the intermediate mode number ($n = 25 - 30$) is large, which indicates that the turbulence inverse cascade is weak. The intermediate mode number generates the inward turbulent transport and spreading. As the pedestal pressure decreases, the dominant modes of the KBM turbulence shift to higher mode number, leading to small initial crash and large radial transport fluxes driven by the KBM turbulence.

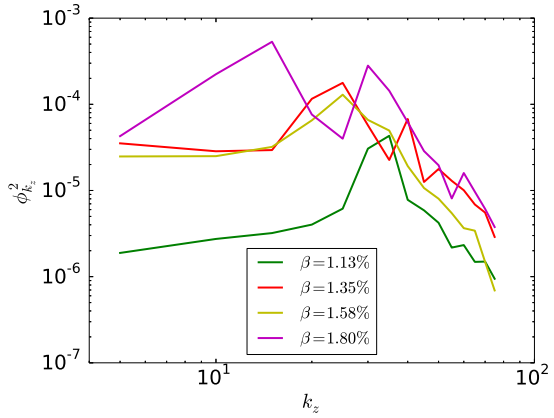

FIG. 13. The time averaged toroidal power spectrum of potential ϕ after the initial crash ($t > 200\tau_A$).

VI. SUMMARY AND DISCUSSIONS

In this paper, we developed 6-field Landau fluid model and 3+1 gyro-Landau-fluid model in the BOUT++ framework. In the simulation of a reduced 6-field model, the ion and electron perturbations have the same strong inward turbulence spreading effect, which soon reaches the inner boundary of the simulations. That means the spreading is caused by the $E \times B$ convection. The Landau resonance prevents the encroachment of the turbulence spreading into the pedestal and core plasmas, leading to a smaller energy loss. The Landau resonance also provides different behavior of ions and electrons, and the suppression of the electron temperature perturbations are weaker. Even when the linear characteristics of the system are fixed, the pedestal density and temperature height can change the inward turbulence spreading effect that has a large impact on the nonlinear transport and total energy loss of ELMs. The energy loss of an ELM decreases when density pedestal height increases, due to the inward turbulence spreading effects. The parallel Landau resonance yields a relatively small cross-phase shift between electron temperature perturbation and $E \times B$ velocity, which causes the difference between ions and electrons. The quasilinear effects during the spreading due to the change of flux-surface-averaged profiles are interesting issues to be studied in the future.

Our 3+1 GLF model is well benchmarked with other gyrokinetic (FULL) and gyrofluid (GLF 3+0) code in the ITG simulations in the limit of $\beta = 0$. From the KBM simulations in BOUT++, we find that the KBM has a smaller growth rate than that of ideal ballooning

mode, which means the kinetic effect has stabilizing effect on the ballooning mode. The global nonlinear β scan shows that the relative energy loss of an ELM increases when β and pedestal height increase. The affected volume of an ELM is large when β is large. There is more inverse cascade on the turbulence in the strongly unstable cases, where the energy loss is large. But the inverse cascade is weak in the marginal unstable case, where an intermediate mode number turbulence dominates. The difference of ions and electrons are also observed in the KBM simulations. The ion drift resonance drives the KBM[16,17] in the finite ion temperature gradient (η_i) regime, which is below the threshold of ideal ballooning mode. The KBM and the induced transport below the threshold of ideal ballooning-mode are important to the rebuilding process of the pedestal after ELMs, and they need to be studied in the future. The KBM turbulence may provide current relaxation and magnetic reconnection, which approach the self-consistent gyrofluid simulation without artificial hyper-resistivity in the future.

ACKNOWLEDGMENTS

The authors wish to acknowledge P. Diamond, A. Dimits, M. V. Umansky, I. Joseph and J. F. Ma for useful discussions. This work was performed under the auspices of the US DoE by LLNL under Contract DE-AC52-7NA27344 and is supported by the ITER-China Program (2013GB111000, 2013GB112006), NSFC (11261140326) and CSC (201206010101). LLNL-JRNL-664403.

REFERENCES

[1]A. Leonard, Phys. Plamsas **21**, 090501 (2014).

[2]F. Wagner, G. Becker, K. Behringer, D. Campbell, A. Eberhagen, W. Engelhardt, G. Fussmann, O. Gehre, J. Gernhardt, G. v. Gierke, G. Haas, M. Huang, F. Karger, M. Keilhacker, O. Klüber, M. Kornherr, K. Lackner, G. Lisitano, G. G. Lister, H. M. Mayer, D. Meisel, E. R. Müller, H. Murmann, H. Niedermeyer, W. Poschenrieder, H. Rapp, H. Röhr, F. Schneider, G. Siller, E. Speth, A. Stäbler, K. H. Steuer, G. Venus, O. Vollmer, and Z. Yü, Phys. Rev. Lett. **49**, 1408 (1982).

[3]P. Snyder, H. Wilson, J. Ferron, L. Lao, A. Leonard, T. Osborne, A. Turnbull, D. Mossessian, M. Murakami, and X. Xu, Phys. Plamsas **9**, 2037 (2002).

[4]P. Snyder, N. Aiba, M. Beurskens, R. Groebner, L. Horton, A. Hubbard, J. Hughes, G. Huysmans, Y. Kamada, A. Kirk, *et al.*, Nucl. Fusion **49**, 085035 (2009).

[5]T. Xia, X. Xu, and P. Xi, Nucl. Fusion **53**, 073009 (2013).

[6]X. Xu, B. Dudson, P. Snyder, M. Umansky, and H. Wilson, Phys. Rev. Lett. **105**, 175005 (2010).

[7]X. Xu, R. Cohen, T. Rognlien, and J. Myra, Phys. Plamsas **7**, 1951 (2000).

[8]X. Q. Xu, M. V. Umansky, B. Dudson, and P. B. Snyder, Communications in Computational Physics **4**, 949 (2008).

[9]T. Xia and X. Xu, Phys. Plamsas **20**, 052102 (2013).

[10]P. Xi, X. Xu, X. Wang, and T. Xia, Phys. Plamsas **19**, 092503 (2012).

[11]Z. Liu, T. Xia, X. Xu, X. Gao, J. Hughes, S. Liu, S. Ding, and J. Li, Phys. Plamsas **19**, 102502 (2012).

[12]J. Ma, X. Xu, and B. Dudson, Nucl. Fusion **54**, 033011 (2014).

[13]X. Xu, J. Ma, and G. Li, Phys. Plasmas **21**, 120704 (2014).

[14]P. Xi, X. Xu, and P. Diamond, Phys. Rev. Lett. **112**, 085001 (2014).

[15]P. Xi, X. Xu, and P. Diamond, Phys. Plasmas **21**, 056110 (2014).

[16]P. Snyder, Ph.D. thesis, Princeton university (1999).

[17]P. Snyder and G. Hammett, Phys. Plasmas **8**, 744 (2001).

[18]P. Snyder, R. Groebner, J. Hughes, T. Osborne, M. Beurskens, A. Leonard, H. Wilson, and X. Xu, Nucl. Fusion **51**, 103016 (2011).

[19]E. Wang, X. Xu, J. Candy, R. Groebner, P. Snyder, Y. Chen, S. Parker, W. Wan, G. Lu, and J. Dong, Nucl. Fusion **52**, 103015 (2012).

[20]D. Dickinson, S. Saarelma, R. Scannell, A. Kirk, C. Roach, and H. Wilson, Plasma Phys. Controlled fusion **53**, 115010 (2011).

[21]W. Wan, S. E. Parker, Y. Chen, Z. Yan, R. J. Groebner, and P. B. Snyder, Phys. Rev. Lett. **109**, 185004 (2012).

[22]D. Fulton, Z. Lin, I. Holod, and Y. Xiao, Phys. Plamsas **21**, 042110 (2014).

[23]G. W. Hammett and F. W. Perkins, Phys. Rev. Lett. **64**, 3019 (1990).

[24]W. Dorland and G. Hammett, Physics of Fluids B **5**, 812 (1993).

[25]M. A. Beer and G. W. Hammett, Physics of Plasmas **3**, 4046 (1996).

[26]P. Snyder and G. Hammett, Physics of Plasmas (1994-present) **8**, 3199 (2001).

[27]H. Sugama, T.-H. Watanabe, and W. Horton, Physics of Plasmas (1994-present) **14**, 022502 (2007).

[28]K. Despain, Ph.D. thesis, University of Maryland (2011).

[29]X. Xu, P. Xi, A. Dimits, I. Joseph, M. Umansky, T. Xia, B. Gui, S. Kim, G. Park, T. Rhee, *et al.*, Phys. Plamsas **20**, 056113 (2013).

[30]P. Xi, X. Xu, T. Xia, W. Nevins, and S. Kim, Nucl. Fusion **53**, 113020 (2013).

[31]A. Dimits, I. Joseph, and M. Umansky, Phys. Plamsas **21**, 055907 (2014).

[32]B. Dudson, M. Umansky, X. Xu, P. Snyder, and H. Wilson, Computer Physics Communications **180**, 1467 (2009).

[33]X.-D. Liu, S. Osher, and T. Chan, Journal of computational physics **115**, 200 (1994).

[34]A. Arakawa, Journal of Computational Physics **1**, 119 (1966).

[35]G. D. Byrne and A. C. Hindmarsh, International Journal of High Performance Computing Applications **13**, 354 (1999).

[36]R. Miller and J. V. Dam, Nucl. Fusion **27**, 2101 (1987).

[37]A. Leonard, T. Osborne, M. Fenstermacher, R. Groebner, M. Groth, C. Lasnier, M. Mahdavi, T. Petrie, P. Snyder, J. Watkins, *et al.*, Phys. Plasmas **10**, 1765 (2003).

[38]A. Ware, P. Terry, P. Diamond, and B. Carreras, Plasma Phys. Controlled Fusion **38**, 1343 (1996).

[39]D. H. E. D. Dubin, J. Krommes, C. Oberman, and W. Lee, Phys. Fluids **26**, 3524 (1983).

[40]M. Beer, Ph.D. thesis, Princeton university (1995).

[41]A. Dimits, G. Bateman, M. Beer, B. Cohen, W. Dorland, G. Hammett, C. Kim, J. Kinsey, M. Kotschenreuther, A. Kritz, *et al.*, Phys. Plasmas **7**, 969 (2000).

[42]G. Rewoldt, Z. Lin, and Y. Idomura, Computer Physics Communications **177**, 775 (2007).